

# Seasonality of the Mesoscale Inverse Cascade as Inferred from Global Scale-Dependent Eddy Energy Observations

JACOB M. STEINBERG,<sup>a</sup> SYLVIA T. COLE,<sup>a</sup> KYLA DRUSHKA,<sup>b</sup> AND RYAN P. ABERNATHEY<sup>c</sup>

<sup>a</sup> Woods Hole Oceanographic Institution, Woods Hole, Massachusetts

<sup>b</sup> Applied Physics Laboratory, University of Washington, Seattle, Washington

<sup>c</sup> Lamont-Doherty Earth Observatory, Columbia University, Palisades, New York

(Manuscript received 15 November 2021, in final form 22 April 2022)

**ABSTRACT:** Oceanic mesoscale motions including eddies, meanders, fronts, and filaments comprise a dominant fraction of oceanic kinetic energy and contribute to the redistribution of tracers in the ocean such as heat, salt, and nutrients. This reservoir of mesoscale energy is regulated by the conversion of potential energy and transfers of kinetic energy across spatial scales. Whether and under what circumstances mesoscale turbulence precipitates forward or inverse cascades, and the rates of these cascades, remain difficult to directly observe and quantify despite their impacts on physical and biological processes. Here we use global observations to investigate the seasonality of surface kinetic energy and upper-ocean potential energy. We apply spatial filters to along-track satellite measurements of sea surface height to diagnose surface eddy kinetic energy across 60–300-km scales. A geographic and scale-dependent seasonal cycle appears throughout much of the midlatitudes, with eddy kinetic energy at scales less than 60 km peaking 1–4 months before that at 60–300-km scales. Spatial patterns in this lag align with geographic regions where an Argo-derived estimate of the conversion of potential to kinetic energy is seasonally varying. In midlatitudes, the conversion rate peaks 0–2 months prior to kinetic energy at scales less than 60 km. The consistent geographic patterns between the seasonality of potential energy conversion and kinetic energy across spatial scale provide observational evidence for the inverse cascade and demonstrate that some component of it is seasonally modulated. Implications for mesoscale parameterizations and numerical modeling are discussed.


**SIGNIFICANCE STATEMENT:** This study investigates the seasonality of upper-ocean potential and kinetic energy in the context of an inverse cascade, consisting of energy transfers to and through the mesoscale. Observations show a scale-dependent cycle in kinetic energy that coincides with temporal variability in mixed layer potential energy and progresses seasonally from smaller to larger scales. This pattern appears dominant over large regions of the ocean. Results are relevant to ocean and climate models, where a large fraction of ocean energy is often parameterized. A customizable code repository and dataset are provided to enable comparisons of model-based resolved and unresolved kinetic energy to observational equivalents. Implications result for a range of processes including mixed layer stratification and vertical structure of ocean currents.

**KEYWORDS:** Eddies; Energy transport; Mesoscale processes; Turbulence; Oceanic mixed layer; Altimetry; Seasonal cycle

## 1. Introduction

Mesoscale turbulence represents a dominant fraction of ocean kinetic energy (KE) and consists of flows that evolve on  $\mathcal{O}(10\text{--}300)$  km spatial scales and week to month time scales (Ferrari and Wunsch 2009). Motions outside of these spatiotemporal bounds can act as sources or sinks of this mesoscale energy. For instance, instabilities of western boundary currents can generate smaller-scale fluctuations like Gulf Stream rings, mesoscale eddies can break apart into smaller filaments with shorter space and time scales, an inverse cascade can import energy from submesoscales [ $\mathcal{O}(1\text{--}10)$  km], and mesoscale motions can merge with mean flows. Efforts to model the ocean and climate system crucially depend on energy transfers within and through the

mesoscale range, with such motions either parameterized or only partially resolved in numerical models. The inverse cascade at mesoscales is one component of a two-part energy cycle: first, available potential energy (PE) is converted to KE at instability scales, and second, KE at small scales is transferred to KE at larger scales. This idealized description of an inverse cascade, however, assumes the flow to be balanced, with competing dynamics playing a minimal role. In reality only some fraction of small scale KE moves to larger scales. The inverse cascade of KE from submesoscales to mesoscales to larger scales is predicted and required by quasi-two-dimensional geostrophic turbulence theory and assumes a steady-state balance between production and dissipation (Kraichnan 1967; Charney 1971; McWilliams 1989). It occurs in the ocean alongside forcings that act across a range of scales and unbalanced motions that can simultaneously precipitate a forward cascade toward dissipation (Roulet et al. 2012). A main source of KE at submesoscales and mesoscales is PE stored in the upper ocean. This PE reservoir, larger in winter due to deepened mixed layers and stronger horizontal density gradients, is a

 Denotes content that is immediately available upon publication as open access.

Corresponding author: Jacob Steinberg, jsteinberg@whoi.edu

DOI: 10.1175/JPO-D-21-0269.1

© 2022 American Meteorological Society. For information regarding reuse of this content and general copyright information, consult the [AMS Copyright Policy \(www.ametsoc.org/PUBSReuseLicenses\)](#).

source of KE converted via baroclinic instability at scales near to or smaller than the first baroclinic deformation radius (Smith and Vallis 2001; Mensa et al. 2013; Sasaki et al. 2014; Callies et al. 2015, 2016; Dong et al. 2020a). Along with horizontal density gradients and mixed layer depths, the conversion of PE to KE varies seasonally, with mixed layer eddies generated via frontal adjustment contributing to springtime vertical restratification (Johnson et al. 2016). Modeling studies have shown this frontal adjustment mechanism for generating eddies at submesoscales to act as a key source of mesoscale energy evolving on both seasonal and longer time scales (e.g., Fox-Kemper et al. 2008).

While the inverse cascade across mesoscales itself has been infrequently observed, its result has been inferred from observations revealing eddy energy-containing scales to be larger than predicted instability scales (Chelton et al. 2007). The inverse cascade is further complicated in a three-dimensional ocean with variable vertical stratification, but modeling studies have shown that an inverse cascade does occur in both barotropic and baroclinic modes and across a range of wavenumbers between instability scales and the Rhines' scale (Scott and Arbic 2007; Serazin et al. 2018). Direct observations of these KE fluxes, however, are limited to either select locations or across spatial scales greater than  $\sim 150$  km (Scott and Wang 2005; Callies and Ferrari 2013).

Spaceborne observations of sea surface height (SSH) provide a means of quantifying ocean KE and eddy kinetic energy (EKE) globally. These measurements have long been used to characterize ocean energetics (Stammer and Dieterich 1999; Scott and Wang 2005; Chelton et al. 2007, 2011; Xu and Fu 2012; Arbic et al. 2013; Rocha et al. 2016), develop eddy censuses (Chelton et al. 2011), and determine the spectral flux of KE across mesoscales (Scott and Wang 2005; Arbic et al. 2014). Analyses often partition ocean KE into time-mean and varying components and/or use gridded altimetry products that reduce horizontal resolution to  $\sim 150$  km due to smoothing associated with interpolation (Taburet et al. 2020). Individual satellite altimeters offer higher spatial resolution, but are still limited by along-track altimeter resolution relative to a latitudinally dependent eddy length scale, instrument noise, track repeat time, and spatial gaps between adjacent tracks. Despite these limitations, recent along-track analysis by Chen and Qiu (2021) show their utility by quantifying the fraction of SSH variability at scales unresolved by gridded products, using spectral methods to partition variance, and finding seasonality in this signal.

Here, a framework is constructed to capitalize on the availability of high-resolution along-track measurements and to apply a scale-aware spatial filtering method. We determine the partitioning of energy across 60–300-km horizontal scales and seasons globally. The methods developed and used in this analysis uniquely permit KE to be partitioned across mesoscales without needing to choose interpolation parameters, such as spatial and temporal decorrelation scales, and windowing or tapering scales required in spectral analysis. These methods complement and extend those of Chen and Qiu (2021) by considering EKE, employing different methods of spatial filtering, interpreting results alongside observations of upper-ocean PE,

and reconciling seasonal patterns with mesoscale turbulence theory. Results reveal regions in the ocean where an imprint of the inverse cascade is apparent, specifically where a seasonal imbalance in the PE to EKE conversion rate appears linked to a scale-dependent seasonal cycle in mesoscale KE. This increased level of spatiotemporal detail regarding the partitioning of KE within the ocean is a crucial part of understanding ocean dynamics and whether numerical models, from regional simulations to global climate models, correctly represent oceanic processes.

## 2. Data

As provided by the Copernicus European Earth Observation program (<https://marine.copernicus.eu>), SSH measurements from three altimeter missions are considered, including a 20-yr (1993–2012) multi-satellite-derived mean sea surface (MSS) estimate. These data are accessed via Pangeo, a cloud-based platform with ready-to-analyze large datasets, such that analysis tools developed here can be used by the community without individually downloading and processing locally. Here we primarily consider measurements from the *Jason-2* mission (j2), with minor comparisons to *SARAL-AltiKa* (al) and *Sentinel-3A* (s3a). In all cases, we use a preprocessed low-pass-filtered variable, “sla\_filtered,” which minimizes instrument error (average SSH error of j2 = 1.1, al = 0.8, s3a = 0.9 cm rms) and has an approximate horizontal resolution of 50, 40, and 40 km for the three satellites, respectively (Taburet et al. 2020; Dufau et al. 2016). *Jason-2* measurements represent the longest available measurement time series of  $\sim 8$  years (2008–15). *SARAL-AltiKa* (2013–19) and *Sentinel-3A* (2016–19) altimeters are both more accurate, with lower rms instrument noise, but occupy orbital tracks less frequently. For additional differences among altimeters, including seasonality in instrument error, see Dufau et al. (2016). Authors specifically highlight altimeter limitations in the Southern Ocean, a region included in this analysis, and confirm resolution capabilities down to  $\mathcal{O}(50)$  km. While differences in altimeter instrument accuracy and mission duration motivate separate analysis for each satellite, statistical properties and spatial patterns of eddy variability are comparable.

Two products derived from Argo float observations are used to estimate the conversion rate of PE to KE. The first is a database of monthly temperature and salinity profiles on a  $1^\circ \times 1^\circ$  grid, created using Argo float profiles collected between 2007 and present (Roemmich and Gilson 2009). The second provides mean monthly mixed layer depth and densities (Holte et al. 2017) and is used to vertically partition density profiles from Roemmich and Gilson (2009). Profiles contributing to the mixed layer depth climatology were collected between 2000 and 2021. This product is used to take advantage of the careful application of mixed layer depth selection criteria and is more accurate than the former product as it is derived from individual profiles rather than a monthly average. These data products represent the climatological state of mesoscale and larger ocean properties.

### 3. Analysis framework

#### a. Scale-aware eddy kinetic energy

The following analysis does not attempt to resolve individual eddy features, but rather geographic and seasonal patterns in velocity variance and EKE. Briefly, we construct a general spatial filtering framework designed to filter any variable along a single spatial dimension. This framework is then applied to cross-track estimates of geostrophic velocity calculated from along-track gradients of absolute dynamic topography (ADT). We then partition observed variance into mean and eddy KE components. While SSH variance can be estimated at a relatively finer horizontal resolution without having to calculate a gradient (and is also useful for model validation purposes), we focus here on eddy energetics.

#### 1) GEOSTROPHIC VELOCITY

The along-track SSH measurements used here are all available with 7-km spacing. Data are first linearly interpolated to 20-km spacing and across intermittent data gap segments of less than 50 km. The choice of 20-km spacing improves the implementation of the spatial filter introduced below. ADT,  $\eta(x, t)$ , represents the dynamical component of the satellite measurement and is defined everywhere as

$$\eta(x, t) = \text{SSH} - \text{MSS} + \text{MDT} = \text{SSH} - \text{MSS} + (\text{MSS} - \text{Geoid}) = \text{SSH} - \text{Geoid}, \quad (1)$$

where, for each unique track,  $x$  is along-track distance in meters,  $t$  is time, MSS is the temporal mean sea surface height, and mean dynamic topography (MDT) is the temporal mean of SSH above the geoid (Pujol and Mertz 2020). The geoid is the baseline surface height of the ocean under the influence of gravity and rotation alone and is included in the MDT estimate. Cross-track geostrophic velocity  $u$  is then estimated as

$$u(x, t) = \frac{g}{f} \frac{\partial \eta}{\partial x}, \quad (2)$$

where  $g = 9.81 \text{ m s}^{-2}$  and  $f$  is the local Coriolis frequency. A negative sign is omitted as we consider only the magnitude of cross-track velocity and its spatial and temporal variability. The along-track gradient of ADT is estimated using a 3-point center difference gradient stencil (Arbic et al. 2012).

Cross-track velocities are calculated for each cycle of each track (Figs. 1a,b) of the desired altimeter. The assumption that these estimates equally represent zonal and meridional components of an isotropic field is justified based on consistency among three altimeters having different orbital track geometries. While the gradient wind balance becomes relevant at smaller scales, no bias as a result of assuming geostrophic balance is expected here because the isotropic assumption implies flows with anticyclonic and cyclonic curvature are equally sampled (Chelton et al. 2011). Comparisons between these estimates and gridded velocities produced by AVISO (not shown) reveal significant differences, largely due to the increased horizontal resolution at which KE can be estimated using along-track measurements.

#### 2) MEAN AND EDDY KINETIC ENERGY

We use spatial filtering to decompose geostrophic velocity into contributions from eddying motions at specific spatial scales. Specifically, for a spatial filter of length  $l$  denoted by  $\langle \rangle_l$ , the eddy kinetic energy at scales smaller than the filter scale (EKE) and mean kinetic energy at scales larger than the filter scale (MKE) are

$$\text{EKE}_l = \tau(u, u)_l = \langle u^2 \rangle_l - \langle u \rangle_l^2, \quad (3)$$

$$\text{MKE}_l = \langle u \rangle_l^2, \quad (4)$$

where small-scale variance  $\tau$  is defined as  $\tau(u, u)_l = \langle u^2 \rangle_l - \langle u \rangle_l^2$  following Germano (1992), Aluie et al. (2018), and Sadek and Aluie (2018). Note that these estimates exclude an along-track velocity component and that a factor of 1/2 is implicit in estimates of KE. This follows from the assumption that the geometries of altimeter orbital tracks result in adequate sampling of both zonal and meridional components of the surface velocity field, and that they are isotropic. This framework prevents the need to define an anomaly quantity (i.e.,  $u' = u - \langle u \rangle$ ) and the need to address the magnitude of cross terms (i.e.,  $\langle u \rangle u'$ ) following substitution into momentum equations. The partitioning of variance into large- and small-scale bins is then framed about the filter scale  $l$ . In practical terms, this filtering framework prescribes set scales across which variance can be partitioned, analogous to resolvable and subgrid variance in an ocean model.

The energy or variance of a field can also be decomposed into  $N$  distinct bands. Let  $\gamma_n$  be the operator that isolates a band. For a single filter, MKE and EKE are given by

$$\text{MKE} = \sum_{n=1}^j \gamma_n(u^2) = \langle u \rangle_{\ell_j}^2, \quad (5)$$

$$\text{EKE} = \sum_{n=j+1}^N \gamma_n(u^2) = \langle u^2 \rangle_{\ell_j} - \langle u \rangle_{\ell_j}^2 = \tau(u, u), \quad (6)$$

where the angle brackets represent the convolution with a filter of length scale  $\ell_1$ . This acts as a low-pass filter, passing variance at scales larger than  $\ell_1$ . For two filter scales, energy within a band bounded by scales  $\ell_1$  and  $\ell_2$  (i.e., a bandpass filter) is

$$\gamma_2(u^2) = \langle u \rangle_{\ell_2}^2 - \langle u \rangle_{\ell_1}^2. \quad (7)$$

For  $N$  bands, we want this to satisfy the integral constraint that

$$\int u^2 dx = \sum_{n=1}^N \int \gamma_n(u^2) dx. \quad (8)$$

The largest-scale energy is defined as

$$\gamma_1(u^2) = \langle u \rangle_{\ell_1}^2. \quad (9)$$

This continues until the highest bands (smallest filter scales):

$$\gamma_{N-1}(u^2) = \langle u \rangle_{\ell_{N-1}}^2 - \langle u \rangle_{\ell_{N-2}}^2, \quad (10)$$

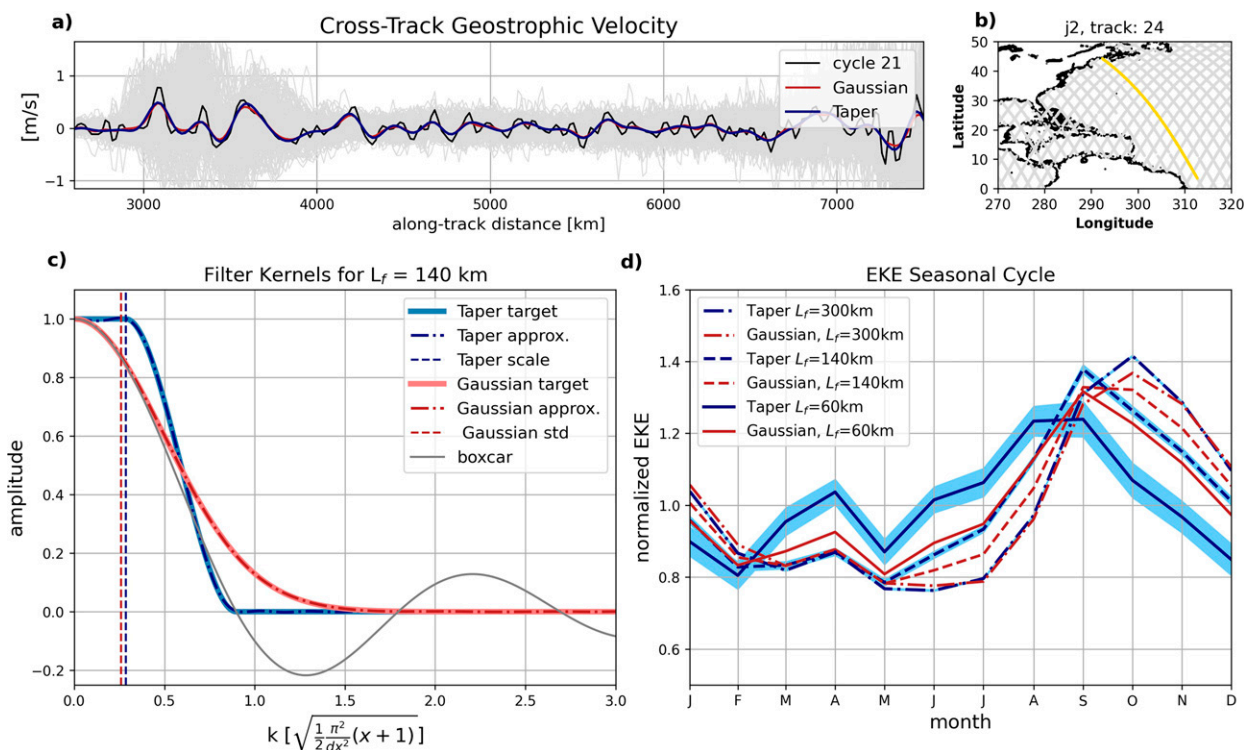


FIG. 1. (a) Cross-track geostrophic velocities (gray) as a function of along-track distance along the *Jason-2* altimeter track 24 from 2008 to 2015 (258 cycles). Track 24 and cycle 21 (black) is selected as an example and filtered using the Gaussian (red) and taper (blue) filters to 140 km. (b) Path over ground of *Jason-2* tracks with track 24 in yellow. Along-track distance increases north to south. (c) Fourier transform of boxcar (black), target and approximate Gaussian (red), and target and approximate taper (blue) filter kernels for a 140-km filter. Horizontal axis is the normalized horizontal wavenumber with  $dx$  and  $x$  the grid spacing and grid indices. Vertical lines identify the normalized filter scale. (d) Seasonal cycle in EKE at  $92^{\circ}\text{E}$ ,  $19^{\circ}\text{S}$  for three filter scales (60, 140, 300 km) and two filter types: taper (blue) and Gaussian (red). EKE at each scale is normalized by its annual mean. The shaded regions are the standard deviation of 250 Monte Carlo simulations showing the effect of random instrument error added to absolute dynamic topography measurements.

$$\gamma_N(u^2) = u^2 - \langle u \rangle_{N-1}^2, \quad (11)$$

where the last band,  $\gamma_N(u^2)$ , is the high-pass filtered energy. For this decomposition, it is straightforward to show that

$$\sum_{n=1}^N \gamma_n(u^2) = u^2. \quad (12)$$

This decomposition of velocity variance into  $N$  distinct bands reveals the partitioning of KE across scales and serves as a discrete analog to the wavenumber spectra (Sadek and Aluie 2018).

### 3) IMPLEMENTATION

Following methods employed by Grooms et al. (2021), a spatial filter is applied to velocity from each cycle of each altimeter track as a convolution of a desired filter kernel with  $u$  as

$$\langle u(x,t) \rangle_l = G_l * u(x,t), \quad (13)$$

where  $G_l$  represents a general filter kernel of width  $l$  with  $n$  number of measurements that span the distance  $l$ . For  $l = 5$

and along-track velocity interpolated to a 20-km grid, the filter would have zero variance at scales less than 100 km. Three filter kernels are considered: boxcar, Gaussian, and taper, each defined to have comparable length scales for a single input  $l$  (Fig. 1). The boxcar filter kernel most simply applies this filtering framework and has a uniform set of weights of width

$$L_f = n\Delta_x, \quad (14)$$

where  $L_f$  is the filter width more generally defined above as  $l$ ,  $\Delta_x$  is the grid step, and filter weights are  $1/n$ . A Gaussian kernel of the same characteristic scale takes the form

$$G_{L_f}(x) = \exp(-6|x/L_f|^2). \quad (15)$$

This expression was selected by considering the Fourier transform of both the boxcar and Gaussian filters and identifying first zero crossings. Equivalently, the taper filter is designed to eliminate contributions from wavenumbers  $k$  greater than  $2\pi/L_f$ . These diffusion-based Gaussian and taper filters employ Laplacian and biharmonic operators to iteratively approximate a target steplike filter constructed in Fourier space using Chebyshev polynomials (Fig. 1). Stability of this smoothing



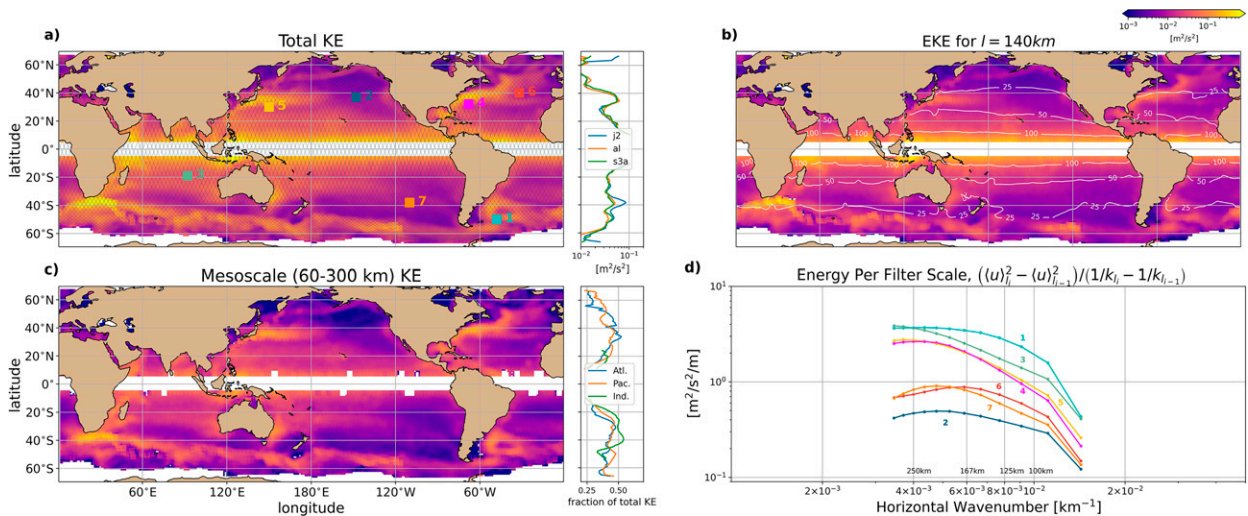


FIG. 2. Gridded maps of (a) mean total KE from *Jason-2* (2009–16) cross-track geostrophic velocity estimates with colored boxes identifying seven select locations individually considered, (b) mean EKE at scales less than 140 km with the first baroclinic deformation radius contoured in white, and (c) mesoscale EKE estimated as the mean KE within the 60–300-km band [Eq. (7)]. In (a), zonal mean total KE for *Jason-2* (blue), *SARAL-AliKa* (orange), and *Sentinel-3A* (green) altimeters is also shown. In (c), the zonal average of KE within the 60–300-km band for the Atlantic (blue), Indian (green), and Pacific (orange) basins is shown as a fraction of mean total KE. White regions in (a)–(c) are those where, at the equator, geostrophy is a poor assumption and, at higher latitudes, where sea ice impacts altimeter measurements. (d) KE within the 60–300-km band at the seven locations identified and numbered in (a). Estimates are normalized by bandwidth. Location details are provided in Fig. 5a.

technique is ensured for filtering scales generally less than 50 times larger than the grid scale and is here no larger than 15 (Grooms et al. 2021).

To make this filtering framework both dynamically relevant and useful in an observation–model comparison, the filter scale  $l$  can be defined in one of three ways: a fixed length scale (e.g., 100 km), a scale tied to a model grid scale (e.g.,  $1^\circ$ ), or a scale tied to a varying dynamical scale (e.g., the first deformation radius  $L_{d1}$ ). The majority of this analysis uses a fixed filter scale and the taper kernel. A fixed length scale is most appropriate for deriving physical meaning from the decomposition of EKE into contributions across scales, while the choice of filtering to the deformation radius would be desirable if the altimeter could resolve  $L_{d1}$  at all latitudes. After estimating total resolvable KE and filtering all cross-track velocity estimates using the taper filter and a fixed length scale, global maps of KE, MKE, and EKE are constructed by bin-averaging along-track fields within  $4^\circ \times 4^\circ$  bins on a  $1^\circ$  longitude–latitude grid (e.g., KE in Fig. 2a).

#### 4) ERROR PROPAGATION

While a filter kernel can be selected to minimize spectral leakage, time-varying instrument error reduces confidence in a seasonal analysis. To approximate the effect of this temporal variability and gain confidence in these results, normally distributed random errors in ADT were added to each cycle of all tracks falling within a  $10^\circ \times 10^\circ$  box (Fig. 2a: green site indicates box center location). For each cycle of each track, 250 Monte Carlo simulations were run, adding random error with a standard deviation equal to the maximum seasonal change in SSH error (Dufau et al. 2016). Cross-track geostrophic velocities were then

estimated, filtering applied, and EKE estimated at three scales. The standard deviation of these 250 runs (shaded green regions in Fig. 1d) reveals added uncertainty in the observed EKE estimate and its scale-dependent seasonal cycle. The signal that we subsequently diagnose, a temporal lag in peak EKE at different scales, is further detailed in the upcoming sections, but remains significant with confidence bounds of approximately  $\pm 1$  month. The effect of this seasonal instrument noise decreases many-fold with increasing filter scale. Monte Carlo error analyses carried out at two additional sites in the North Pacific (not shown) exhibit similar standard deviations across 250 runs and suggest these error estimates are representative despite expected spatial variability in instrument errors.

#### b. Available potential energy and conversion to kinetic energy

We estimate the mean conversion rate of PE to submesoscale EKE,  $\overline{w'b'}$ , using an often employed parameterization since it is not possible to directly estimate it from observations. The parameterization of Fox-Kemper et al. (2008) and Fox-Kemper et al. (2011) diagnoses a PE to EKE conversion rate as

$$\overline{w'b'} = \frac{\Delta s}{L_f} \frac{H^2}{|f|} \left[ \left( \frac{\partial b}{\partial x} \right)^2 + \left( \frac{\partial b}{\partial y} \right)^2 \right], \quad (16)$$

where  $H$  is the mixed layer depth,  $f$  is again the local Coriolis parameter, and buoyancy  $b = -g(\rho - \rho_0)/\rho_0$ . The first term in this equation,  $\Delta s/L_f$  is a scaling factor recommended by Fox-Kemper et al. (2011) to account for the sensitivity of this estimate to the distance ( $\Delta s$ ) over which horizontal buoyancy

gradients are estimated relative to the horizontal scale of mixed layer instability ( $L_f = NH/|f| \approx |\nabla_h b|H/f^2$ ). These choices are intended to produce an estimate representative of mesoscale fronts that drive mixed layer instabilities (Johnson et al. 2016; Uchida et al. 2017). Johnson et al. (2016) characterize these large-scale gradients as comprised of smaller-scale and sharper-gradient fronts susceptible to baroclinic instability, while Uchida et al. (2017) use a high-resolution model to show that conversion estimates calculated from time-dependent mesoscale gradients are representative of direct flux estimates. Overall, this parameterization reveals when and where PE stored in mixed layer fronts is converted to EKE via mixed layer baroclinic instability.

We use Argo-derived upper-ocean density climatologies to estimate the horizontal buoyancy gradients and mixed layer depths needed for Eq. (16). Horizontal buoyancy gradients are estimated at 19 m depth and across 2° distances. In Eq. (16),  $\Delta s$  varies latitudinally as the distance, in meters, of 2° of longitude, and the length scale of instability  $L_f$  has typical values from a few hundred meters to a few kilometers. Two locations, one in the western North Atlantic and one in the western South Atlantic, highlight the distinct seasonal cycles of mixed layer depth, horizontal buoyancy gradients, and PE to EKE conversion (Fig. 3). In particular they show the differing contributions to this conversion estimate of horizontal buoyancy gradient changes and mixed layer depth changes. These sites were selected to highlight differences in upper-ocean seasonality. While mixed layer depths at the South Atlantic site change seasonally by almost 200 m, horizontal buoyancy gradients are weaker such that the conversion rate has a similar peak amplitude to the site in the North Atlantic, where mixed layer depth changes are smaller and horizontal buoyancy gradients stronger. In both cases, the seasonal change in conversion rate is comparable to or larger than the annual mean conversion rate.

## 4. Results

### a. Mesoscale eddy kinetic energy across seasons and scales

By filtering geostrophic velocities using the taper filter, we estimate MKE and EKE across different horizontal scales and seasons. We calculate MKE [Eq. (4)] and EKE [Eq. (3)] at length scales  $l = 60\text{--}300$  km in 20-km intervals and first generate global maps of KE (Fig. 2a), MKE, and EKE (shown for  $l = 140$  km in Fig. 2b). KE within the 60–300-km band is estimated by summing across wavenumbers spanning our chosen filtering band (Figs. 2c,d). This set of filter scales includes the smallest scales resolved by the altimeter and extends up to the larger mesoscales. We refer to energy at specific scales wherever possible, with the 60–300-km band approximating the mesoscale energy in much of the region equatorward of 60°. Because the deformation radius varies with latitude, the 60–300-km band does not include the smallest scales within the mesoscale poleward of approximately 20°. Although our results do not focus on the region equatorward of approximately 20°, here the 60-km scale represents the uppermost

scales of the submesoscale energy band. These issues are discussed further in section 5.

Several aspects of KE are geographically variable (e.g., Fig. 2). Consistent with prior studies, total KE in the Antarctic Circumpolar Current and western boundary current regions is over an order of magnitude more energetic than in eastern ocean basins. MKE, or the energy at and above a certain filter scale, generally decreases with increasing filter length scale, but the rate of this decrease, akin to a spectral slope, also varies with location (Fig. 2d). Specific locations were selected for illustrative purposes to consider variability in each ocean basin, at a variety of latitudes, and at sites both energetic and quiet. Within the 60–300-km range, here defined as the mesoscale band, slopes are steeper where eddy energy is high. In other words, the partitioning of energy across scales varies geographically. The result is a varying fraction of KE contained within the mesoscale band, with values approaching 50% of total resolvable KE in western boundary current regions (Fig. 2c). The fraction of energy contained in this mesoscale band decreases near the equator and at latitudes greater than  $\sim 45^\circ$ , where deformation radii fall outside the upper (equator) and lower (high latitude) limits of our 60–300-km band.

Seasonal variability is first considered by estimating the fraction of KE within two wavelength bands (60–140 and 140–300 km) in late Northern Hemisphere winter [February–April (FMA)] and summer [July–September (JAS)] months (Figs. 4a–e). The choice of 140 km as the scale to divide this wavenumber band reflects the intent to consider small- and large-scale KE separately, with the smaller band encompassing motions no larger than twice the deformation radius. The results are not sensitive to the choice of 140 km. These months were selected to align with months of maximal and minimal KE at scales less than 140 km. In the Northern Hemisphere, the fraction of energy at 60–140-km scales is elevated outside of western boundary current regions, and is overall larger in wintertime (Fig. 4c). At 140–300-km scales, western boundary current regions have a larger fraction of energy at these scales during summertime (JAS in the Northern Hemisphere, FMA in the Southern Hemisphere; Figs. 4d,e). From this basic partitioning, it is clear that the seasonality of ocean KE is scale dependent (i.e., it differs at large and small spatial scales).

The largest winter-to-summer differences of approximately 25% variation occur in the 60–140-km band, equatorward of western boundary currents (Fig. 4c). The finding that energy at 60–140-km scales peaks in late winter is consistent with the theory that submesoscale EKE can act as a time-dependent source of mesoscale EKE that reaches the mesoscale via the inverse cascade (Qiu et al. 2014; Callies et al. 2015; Uchida et al. 2017; Dong et al. 2020b). At 140–300-km scales, differences between winter (FMA) and summertime (JAS) KE are smaller in magnitude (Fig. 4f), as the months of maximal and minimal KE at these scales often occur in other months such that these winter and summertime periods do not represent the full seasonal change. The Agulhas Current region is an exception, with significantly elevated KE in Southern Hemisphere winter, consistent with prior studies (Matano et al. 1998). Overall, this observed seasonality compares favorably to previous observational studies, which have been

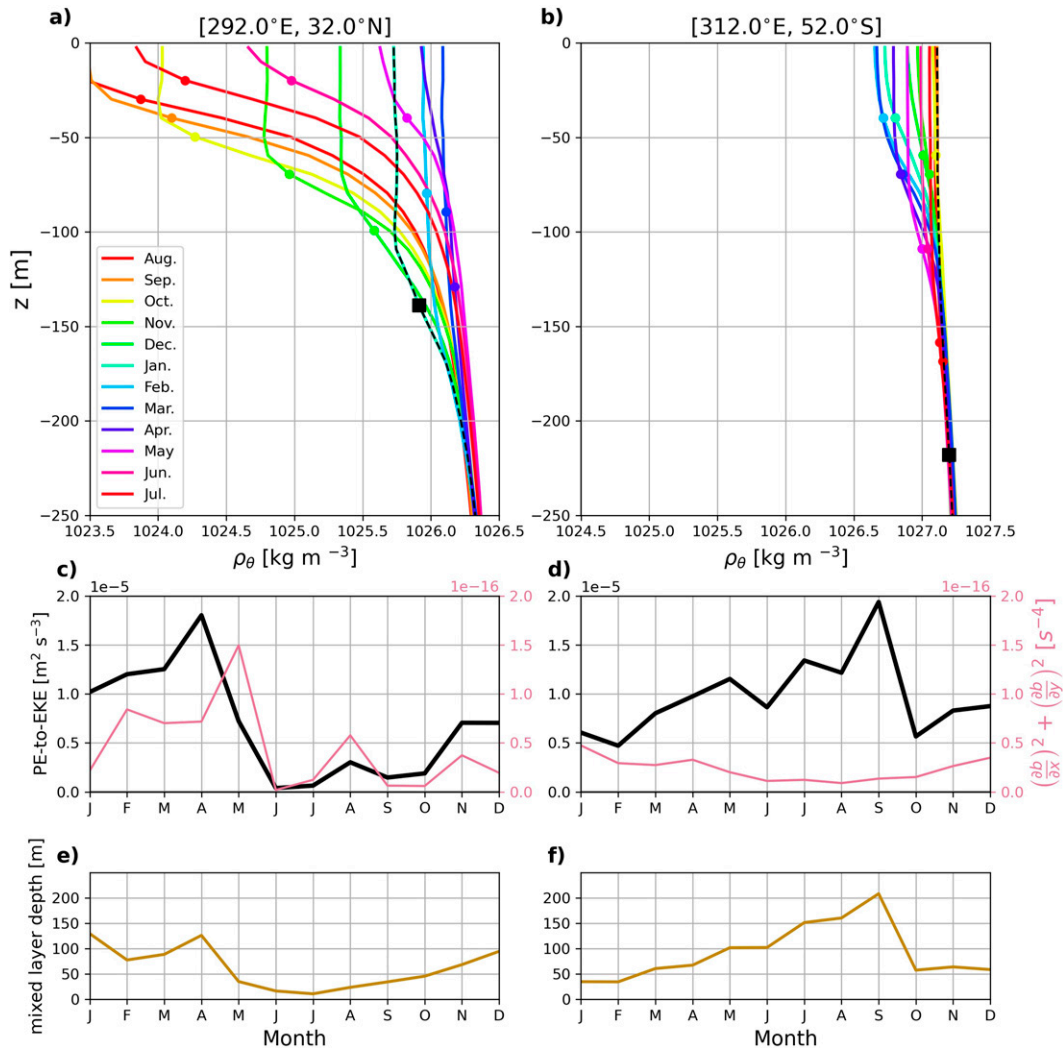


FIG. 3. Upper-ocean density profiles for each month in (a) the western North Atlantic Ocean (32°N, 292°E) and (b) the southwestern Atlantic Ocean (52°S, 312°E) from Argo float observations (Roemmich and Gilson 2009). Colored circles identify mixed layer depth for each month with the black square denoting the deepest mixed layer depth. The black dashed line is the corresponding density profile. Seasonal cycle of the PE to EKE conversion rate [black; Eq. (16)] and sum of squared horizontal buoyancy gradients (pink) at (c) 32°N, 292°E and (d) 52°S, 312°E. Seasonal cycle of mixed layer depth at (e) 32°N, 292°E and (f) 52°S, 312°E.

limited to analysis of a single mesoscale range typically larger than 150 km (e.g., Scharffenberg and Stammer 2010).

A mean seasonal cycle for each filter scale is constructed by partitioning filtered velocities from all altimeter tracks into monthly bins before averaging into latitude-longitude bins. Seven locations spanning all ocean basins are selected to highlight the mean seasonal cycle for three filter scales (60, 140, 300 km; Fig. 5). At a subset of these example locations (Figs. 5e,g,h), a progression in the month of maximum EKE is identified, with the peak occurring first at small (60 km), then medium (140 km), and finally large (300 km) scales. This progression reveals a scale-dependent shift in the seasonal cycle of EKE, with the difference in peak EKE month identified as a temporal lag. Among the selected sites, not all exhibit this

sequence of events (Figs. 5c,d,f,i). At these locations, a seasonal cycle is often observed but is similar at all spatial scales (peak EKE occurs in the same month). These examples show that the amount of total KE does not determine whether or not a region exhibits a scale-dependent shift in the seasonal cycle of EKE.

To investigate global patterns, we consider the peak month of PE to EKE conversion rate (Fig. 6a),  $EKE_{\leq 60km}$  (Fig. 6b), and  $EKE_{60-300km}$  (Fig. 6c). At many locations, a seasonal progression from  $EKE_{\leq 60km}$  to  $EKE_{60-300km}$  is apparent (Fig. 6b,c), even in regions with relatively little total KE (Fig. 2a). At scales less than 60 km, peak EKE occurs in wintertime months. At 60–300-km scales, spatial variability in the month of maximal EKE is more pronounced, with western boundary current regions peaking



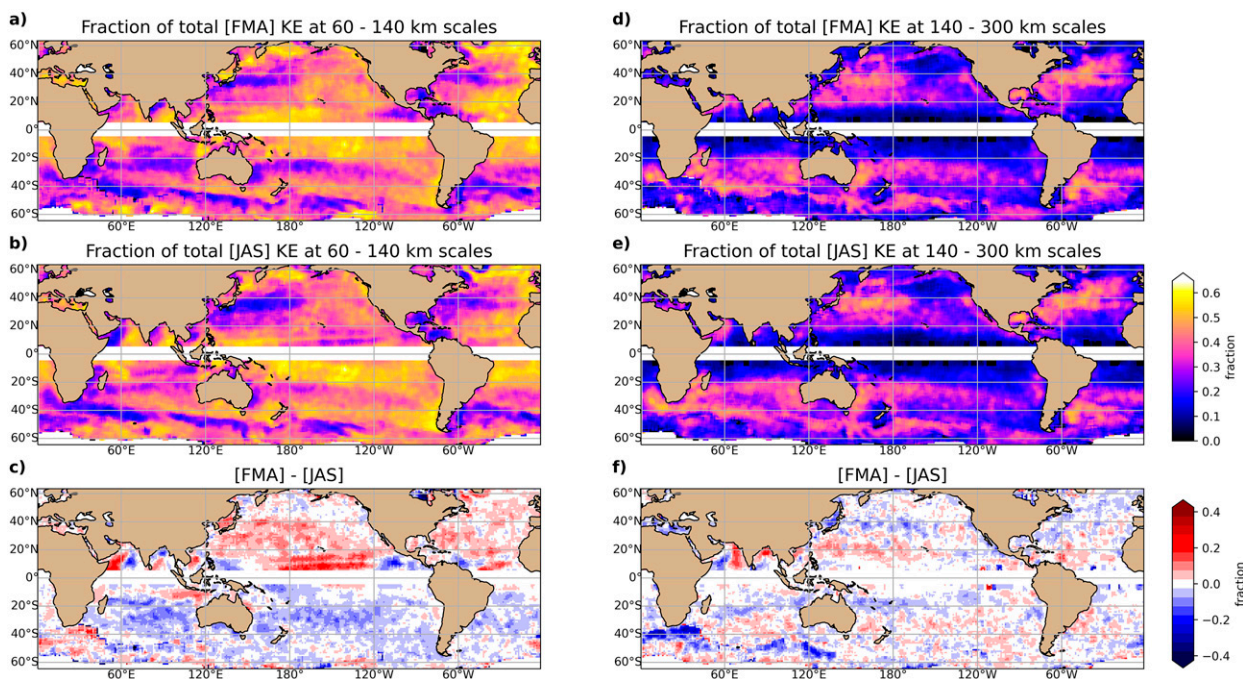


FIG. 4. Fraction of (a) FMA and (b) JAS total KE in the 60–140-km band. (c) FMA fraction minus JAS fraction. (d)–(f) as in (a)–(c), but for 140–300-km scales.

several months later than neighboring gyre regions. The difference in the month of maximal  $EKE_{\leq 60\text{km}}$  and maximal  $EKE_{60-300\text{km}}$  (Fig. 6e) reveals large-scale geographic patterns in a scale-dependent seasonal cycle of EKE. Throughout much of the midlatitudes,  $\sim 20^\circ\text{--}40^\circ$ , as well as in the subpolar North Atlantic, this lag is positive and between 1 and 4 months (Fig. 6e, orange regions). Lags are only shown where the amplitude of the seasonal cycle exceeds 25% of its annual mean value, a criterion satisfied at  $\sim 95\%$  of locations. Lags appear greatest in the eddy recirculation region of the subtropical gyres, compared to the eastern North Pacific or South Atlantic where lags approach zero or do not have a definitive sign. Regions with lags outside of the 1–4 month range are found closer to the equator, in the North Pacific north of  $40^\circ\text{N}$ , and south of  $45^\circ\text{S}$  where deformation radii are outside the 60–300-km scale range considered here.

In summary, large regions of the global ocean, with both high and low levels of mesoscale KE, appear to experience a seasonal cascade of energy from the smallest scale resolvable by the altimeter to  $\sim 300\text{-km}$  scales. Here, the observed difference in seasonal cycles between  $EKE_{60-300\text{km}}$  and  $EKE_{\leq 60\text{km}}$  (Fig. 6) reveals a temporal lag consistent with predictions as to the inverse cascade and prior modeling results (Qiu et al. 2014; Dong et al. 2020b).

#### b. Seasonal variations of available potential energy and conversion to kinetic energy

The seasonal cycle in the PE to EKE conversion rate is independently estimated from observations to aid interpretation of EKE seasonality and scale dependence. Temporally, this conversion rate exhibits a distinct peak during specific winter

months, often aligning with  $EKE_{\leq 60\text{km}}$  (Fig. 5). Both the mean and seasonal amplitude of this estimated rate are elevated in subtropical western boundary current regions, the subpolar North Atlantic, and the Southern Ocean (Fig. 7), with the seasonal amplitude often larger than the annual mean. The PE to EKE conversion rate is a proxy for EKE generation at submesoscales. We argue that some of this submesoscale energy likely moves upscale, and thus that understanding seasonal modulations in the PE to EKE conversion rate is important in understanding and modeling mesoscale motions.

To relate the seasonality of the PE to EKE conversion rate to that of small and larger-scale EKE, we first consider the seven locations highlighted in Fig. 5. The PE to EKE conversion rate is elevated in specific winter months, but remains nonzero throughout the year. This pattern is interpreted as an increased pool of PE susceptible to baroclinic instability, which, as implied by Fox-Kemper et al. (2008), occurs principally at scales smaller than the deformation radius. At many locations, this expectation is corroborated by the fact that the conversion rate reaches its elevated wintertime level in the months preceding or at the same time as the peak EKE at scales less than 60 km. At sites where the PE to EKE conversion rate peaks before EKE at any scale, the subsequent progression in EKE across increasing scales follows (Figs. 5e–h). At sites where this does not occur, the seasonal cycles in mixed layer PE and EKE may be related via different dynamics such as a forward cascade of KE.

In general, if mixed layer instability generates small-scale EKE as quantified by Eq. (16) (Fig. 7), we would expect geographic overlap between regions with seasonality in PE to EKE conversion and EKE at small scales. If this EKE then moves to larger



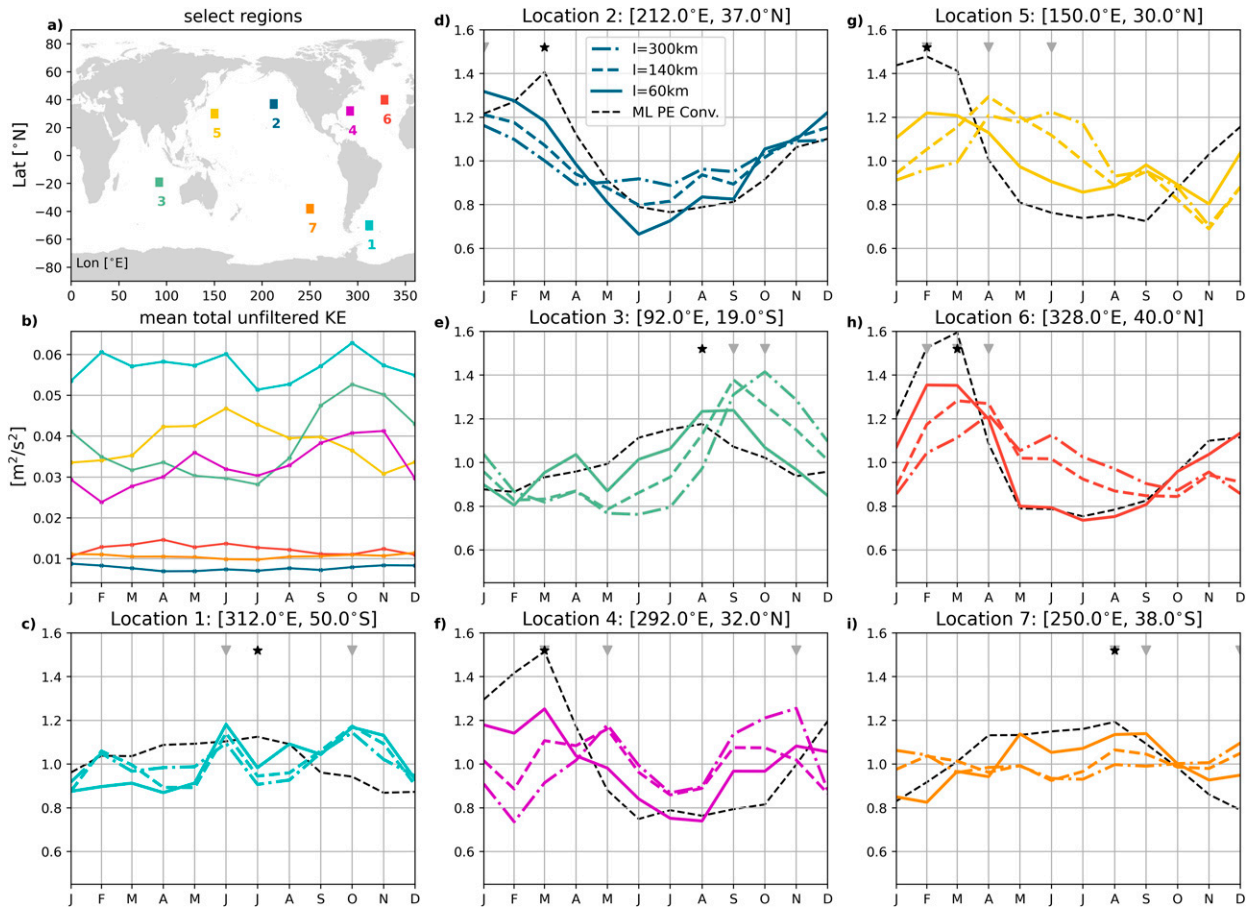


FIG. 5. Mean seasonal cycle as a function of scale at seven select locations (same locations as in Fig. 2). (a) Map of locations. (b) Mean seasonal cycle of total KE at each location. (c)–(i) Mean seasonal cycle of EKE normalized by its annually averaged value for 300 km (dash-dot), 140 km (dash), and 60 km (solid) filter scales. Black line (dashed) is the PE to EKE conversion rate normalized by its annual average. Symbols identify the month of peak conversion (star) and peak  $\text{EKE}_{60\text{km}}$ ,  $\text{EKE}_{140\text{km}}$ , and  $\text{EKE}_{300\text{km}}$  (downward triangles).

scales via the inverse cascade, we would expect geographic overlap among regions with seasonality in PE to EKE conversion, seasonality in EKE at small scales, *and* seasonally lagged EKE at large scales. We first investigate the geographic overlap where the seasonal amplitude of the conversion rate is greater than its annual mean (Fig. 7) and where the seasonal amplitude in EKE at 60–140-km scales, expressed as a fraction of total KE, is greater than its annual mean (Figs. 8a,b). These independently estimated quantities are both elevated throughout the midlatitude gyres (Fig. 8b). Regions where this overlap occurs are interpreted as experiencing both a strong seasonal cycle in PE to EKE conversion and in resolved EKE at scales closest to those energized via the conversion of PE to KE. Within regions of this overlap, nearly 50% of EKE lag estimates (Fig. 8c) are between one and four months while outside of these regions, this percentage drops to less than 20%. We next compare regions where the seasonal amplitude of the PE to EKE conversion rate exceeds its annual mean and where we observe a positive lag of 1–4 months between peak  $\text{EKE}_{\leq 60\text{km}}$  and peak  $\text{EKE}_{60-300\text{km}}$  (Figs. 8c,d). Again, the midlatitude

gyres stand out as regions of overlap (Fig. 8d). The alignment of these overlap regions (Figs. 8b,d) suggests a correspondence between the seasonal cycle in EKE across mesoscales and the presumed source of this energy: PE stored in the upper ocean. While we are unable to resolve EKE at and below deformation radius scales, spatial patterns in the lag between month of peak PE to EKE conversion and month of peak  $\text{EKE}_{\leq 60\text{km}}$  align with regions where we also observe a 1–4-month lag between  $\text{EKE}_{\leq 60\text{km}}$  and  $\text{EKE}_{60-300\text{km}}$ .

To summarize, regions of strongly seasonal elevated conversion rates identify the presence of submesoscale EKE. Within these regions, specifically within midlatitude gyres, altimeter-observed small-scale EKE is also elevated and nearly in phase with Argo-derived conversion rates (white areas in Fig. 6d). Furthermore, these same locations stand out as where the time lag between seasonal maxima in EKE, defined above, is positive (orange areas in Fig. 6e). Combined, these results are consistent with the hypothesis that mesoscale KE in these regions is at least partly derived from smaller-scale KE generated via mixed layer baroclinic instability that then moves upscale via the inverse cascade.

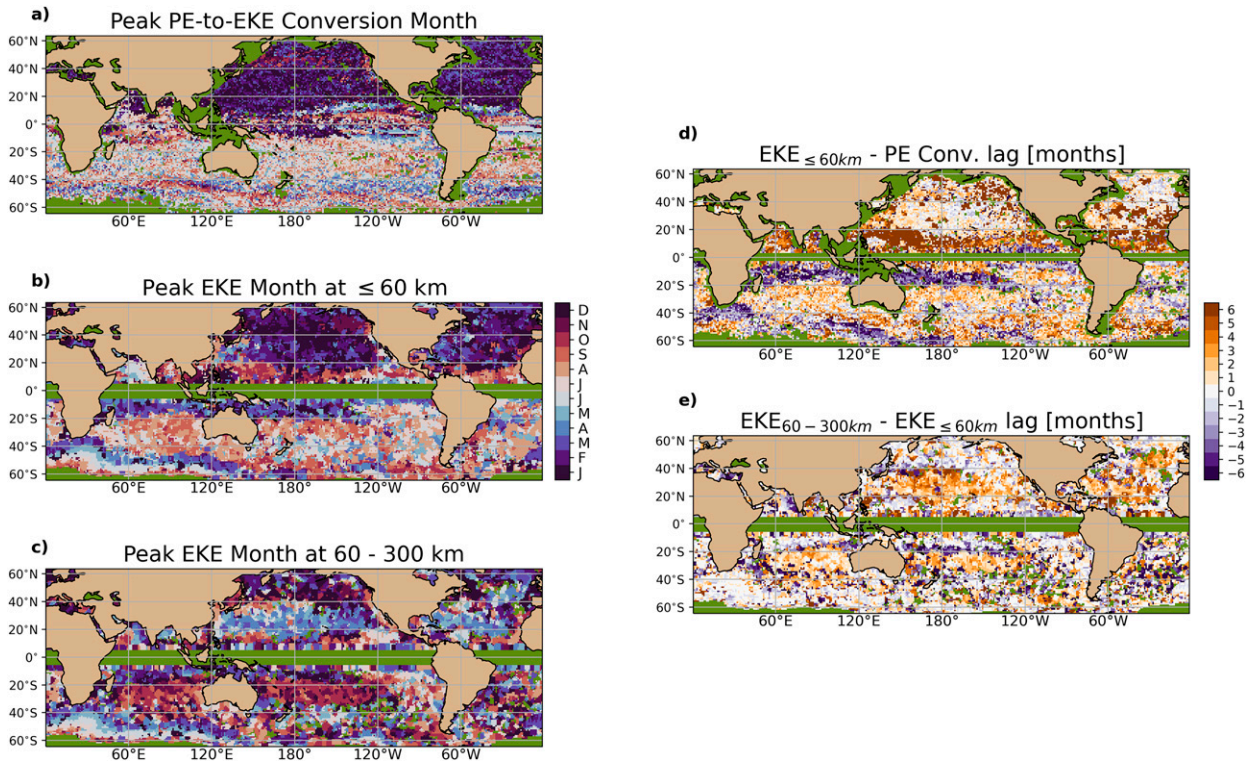


FIG. 6. Month of maximum (a) PE to EKE conversion, (b)  $EKE_{\leq 60\text{km}}$ , and (c)  $EKE_{60-300\text{km}}$ . Temporal lag, in months, between (d) peak  $EKE_{\leq 60\text{km}}$  and peak PE to EKE conversion rate, and (e)  $EKE_{60-300\text{km}}$  and  $EKE_{\leq 60\text{km}}$ . Green regions are those omitted from the lag calculation, including where the total seasonal range in EKE at  $<300\text{-km}$  scales is less than 20% of the annual mean EKE. White and light orange regions in (d) identify where the conversion from PE to EKE occurs at the same time or just prior to the peak in EKE at small scales. These regions correspond to the orange regions in (e) where the peak in EKE at large scales follows the peak in EKE at small scales by 1–4 months.

Outside of these regions of overlap (blue regions in Figs. 8b,d), mesoscale turbulence may be less energetic, forced at larger scales, and/or driven by factors other than seasonal variability.

## 5. Discussion

### a. Interpretation as an inverse cascade

We interpret these results as indirect observation of the inverse cascade through two pieces of evidence. The first is a 1–4-month lag between the seasonal peak of  $EKE_{\leq 60\text{km}}$  and  $EKE_{60-300\text{km}}$ . The second is that seasonality in an independent estimate of PE to EKE conversion peaks at the same time as small-scale EKE and is elevated in regions where EKE lags are positive. Overall, observed PE to  $EKE_{\leq 60\text{km}}$  lags of 0–2 months and  $EKE_{\leq 60\text{km}}$  to  $EKE_{60-300\text{km}}$  lags of 1–4 months occur in overlapping regions (Figs. 6d,e). In these regions, we identify a progression in the month of peak PE to EKE conversion,  $EKE_{\leq 60\text{km}}$ ,  $EKE_{\leq 140\text{km}}$ , and finally  $EKE_{\leq 300\text{km}}$ . These features are consistent with high-resolution modeling studies that explicitly diagnose seasonality in the strength of the inverse cascade (Qiu et al. 2014; Sasaki et al. 2014; Uchida et al. 2017).

We emphasize that the results and evidence for an inverse cascade are not overly dependent on the choice of scales in the

present analysis. The scales chosen here (60, 140, and 300 km) illustrate the seasonality and scale dependence of KE in the ocean. We have estimated MKE and EKE at a range of scales, including the deformation radius, degree resolution for comparison with model output, and a variety of fixed length scales (see the data availability statement), and find that the geographic patterns are generally insensitive to the scale.

It is presumed that seasonal mixed layer PE, deriving from wintertime mixed layer deepening and elevated horizontal buoyancy gradients, is a source of EKE predominantly at scales smaller than those resolved by along-track altimeter observations. Where an inverse cascade is local and moves this energy to larger scales, we expect geographic alignment in the PE to EKE conversion rate and small-scale EKE resolved here. This expectation is tested by considering the intersection of regions where the seasonal cycle in the rate of PE to EKE conversion is large and where significant seasonality in EKE at 60–140-km scales is observed (Fig. 8b). The resulting overlap suggests a dynamical correspondence between these independent observations linking the reservoir of PE in the upper ocean, strong seasonality in small-scale EKE, and a progression in the month of peak EKE first at small and then large scales. These observations reveal an energy cycle that can be sequentially interpreted as: a wintertime increase in PE to EKE conversion, driven by deeper wintertime

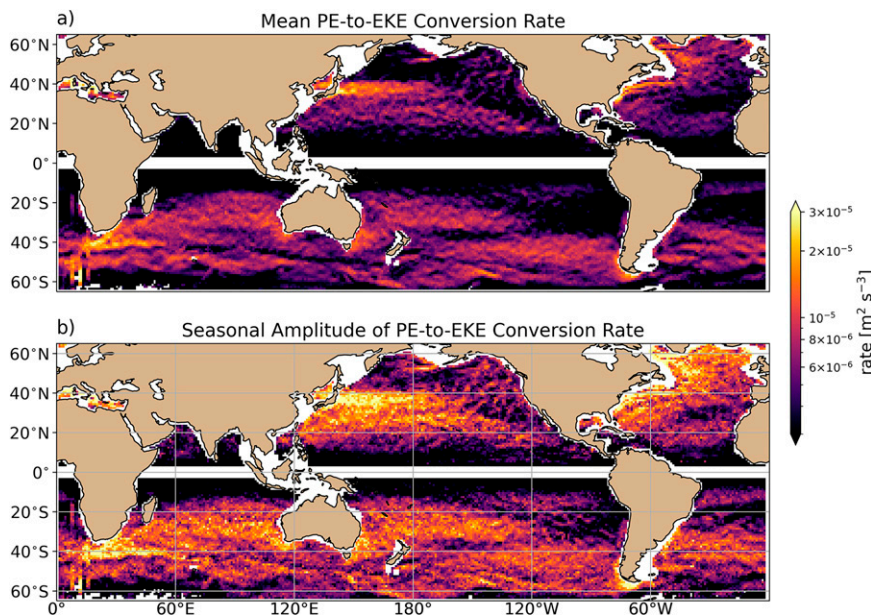


FIG. 7. (a) Mean PE to EKE conversion rate. (b) Seasonal amplitude (maximum–minimum) of the PE to EKE conversion rate.

mixed layers susceptible to baroclinic instability in the presence of stronger lateral buoyancy gradients, followed by elevated eddy activity at scales less than or equal to the first baroclinic deformation radius (Smith 2007), and finally an inverse cascade of KE up to altimeter-resolved scales evidenced by a lag in the month of peak  $\text{EKE}_{\leq 60\text{km}}$  preceding that of  $\text{EKE}_{60-300\text{km}}$ .

Geographic patterns in PE to EKE conversion specifically align with regions where a majority of springtime restratification is generated via the lateral slumping of horizontal density gradients (Johnson et al. 2016). In their analysis, Johnson et al. (2016) discuss the contribution to this conversion of horizontal density gradients to vertical density gradients by mixed layer eddies (Fig. 4 of Johnson et al. 2016). The formation of these eddies, representing the conversion of PE to EKE, in regions where we observe a 0–2-month lag between peak PE to EKE conversion and  $\text{EKE}_{\leq 60\text{km}}$  (Fig. 6d) lends support to our interpretation that the smallest-scale EKE observed by the altimeter reflects energy derived from mixed layer baroclinic instability. The relatively short lag suggests this energy moves upscale at the  $\sim 1$ -month time scale. This result is consistent with Uchida et al. (2017), who calculated a 40–50-day eddy turnover time scale for regions with elevated eddy activity. In these same regions we observe a lag of 1–4 months between peak EKE at  $\leq 60$ -km scales and between 60- and 300-km scales. Interpreted together, these regions identify where geostrophic turbulence drives an inverse cascade from submesoscales through mesoscales. Note that these regions are a conservative estimate of where the inverse cascade occurs. It may additionally be present in other locations with decreased seasonality or at a faster pace such that no perceptible time lag is identified from monthly observations. The sequence of peaks interpreted here as evidence of an inverse cascade does not suggest the absence of a forward cascade, especially at scales equal to and smaller than

$\sim 60$  km and in regions with observed lags of 0–4 months. Instead, we argue that the progression from conversion scale to three subsequently larger wavelengths within the mesoscale (Figs. 5e,g,h) cannot be explained by independent forcings, but rather is the result of an inverse cascade.

Several studies have documented a link between mixed layer instability and mesoscale EKE. Using a high-resolution realistic numerical simulation of the North Pacific, Sasaki et al. (2014) consider additional sources, including Charney-like and Phillips-like instability processes, and conclude that seasonally varying mixed layer instability is a dominant source of mesoscale EKE. Both high-resolution simulations (Mensa et al. 2013) and observations in the North Atlantic (Callies et al. 2015) have shown a correspondence between mixed layer depth and submesoscale EKE. This correspondence aligns with the temporal patterns of mixed layer PE and small-scale EKE shown here.

Other sources of mesoscale KE are considered unlikely to cause the pattern of lag shown here. Investigating the temporal offset between seasonal cycles of EKE and its presumed energy source mechanism, baroclinic instability, Zhai et al. (2008) rule out seasonal variations in Ekman pumping as a driver of EKE seasonality. Their results can be reinterpreted by acknowledging that their observed summertime peak in EKE is defined relative to a temporal mean. This likely corresponds to peak EKE at large scales while small-scale EKE, contributing less to total KE, peaks earlier in the year and closer to their observed time of peak eddy growth rate. Other sources of mesoscale KE that may be seasonally varying, like large-scale wind forcing or baroclinic instability at scales greater than the deformation radius, are considered unlikely to cause the pattern of lag shown here. Wind forcing and its seasonal variability largely occur at basin scales, and although surface ocean temperature fronts can alter the



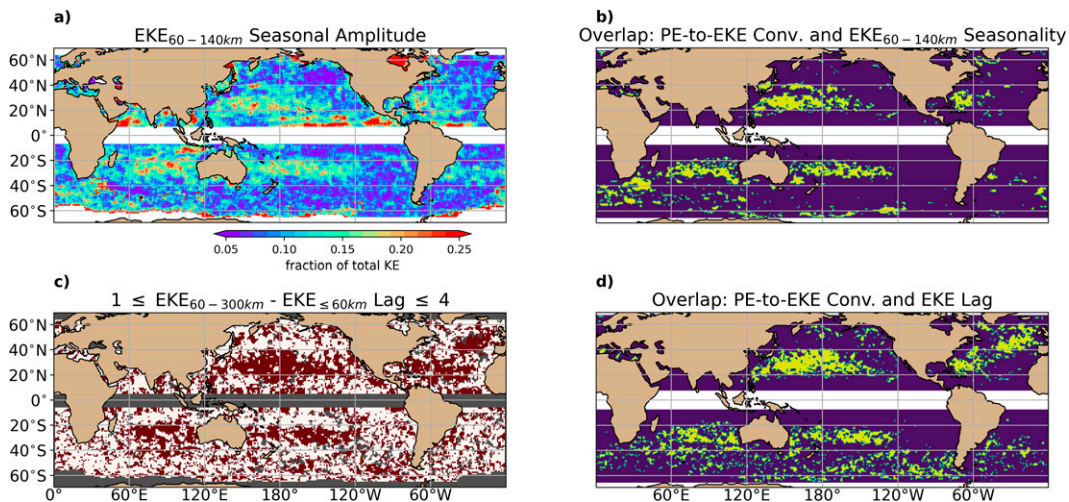


FIG. 8. (a) Seasonal amplitude of the fraction of KE within the 60–140-km wavelength band. (b) Regions (yellow) where the seasonal amplitudes in the PE to EKE conversion rate and fraction of  $EKE_{60-140km}$  exceed their annual mean values. (c) Regions (red) where the lag between peak  $EKE_{\leq 60km}$  and  $EKE_{60-300km}$  is greater than or equal to 1 month and less than or equal to 4 months. (d) Regions (yellow) where the seasonal amplitude in the PE to EKE conversion rate exceeds the annual mean and EKE lags fall between 1 and 4 months.

wind field at mesoscales, these feedbacks do not appear to have widespread seasonal scale dependence (Risien and Chelton 2008; Serazin et al. 2018).

In high-resolution simulations south of the Kuroshio, Sasaki et al. (2014) and Qiu et al. (2014) consider mesoscale KE and the influence of interior baroclinic instability. The authors conclude that contributions to larger-scale KE include a seasonally dependent upscale cascade as well as a persistent source of EKE associated with vertically sheared mean flows. However, the seasonal amplitude of KE at these larger scales associated with interior instability is weaker than that at smaller scales. Sasaki et al. (2014) conclude from this that most of the KE in the mesoscale band is affected by seasonality generated in wintertime at submesoscales.

Implicit in these arguments is the assumption that SSH anomalies used in estimating KE reflect predominantly balanced motions. Qiu et al. (2014) identify spatial variability in the transition scale between balanced and unbalanced motions, revealing much of the EKE at midlatitudes, especially within the western halves of ocean basins, to reflect balanced motions. These regions again align with those here associated with a lag in the peak month of EKE, suggesting that the progression in EKE is not the result of seasonally varying unbalanced motions. The correspondence of locations of lag in EKE from smaller to larger scales and locations of both increased wintertime mixed layer PE conversion and small-scale EKE provide additional support to the argument that these lags identify regions where geostrophic turbulence moves energy from smaller to larger scales.

A scale energy flux could be directly estimated if both components of the horizontal velocity field were resolved along with their zonal and meridional gradients. These estimates have been made in high-resolution simulations (Schubert et al. 2020), but at present, even gridded altimeter fields are inadequate as gridding introduces scale-dependent biases.

#### b. Implications and practical applications

The generalized spatial filtering framework applied here is applicable to any along-track observation. Satellite, time window, filter length scale including degree or kilometer options, filter kernel, and gridding scheme parameters can be varied in this scale-aware framework to explore specific questions or compare to model output. A resulting dataset and example code have been made publicly available, and we encourage its use. As a contribution to the current Ocean Transport and Eddy Energy Climate Process Team (Zanna 2019; Cole et al. 2020), this analysis framework is intended to aid in efforts to partition energy across reservoirs and regulate cross-scale transfers using parameterizations.

Comparison of boxcar, Gaussian, and taper filters reveals the taper filter as the sharpest in spectral space. As a low-pass filter with a cutoff wavelength of  $L_f$ , this kernel most closely approximates a step function in wavenumber space (Fig. 1c). Use of this filter thus produces a field with the least smearing of wavelengths across scales. The effect of this design and result of its implementation, as compared to equivalent analysis using a Gaussian filter kernel, reveal a more distinct signal of seasonality in EKE at different scales. In particular, the month of peak EKE at any given scale is more pronounced and sometimes different for the taper filter than the Gaussian filter (Fig. 1d).

This framework and data processing can be applied to filtered sea level anomaly, cross-track geostrophic velocity, or an arbitrary 1D scalar field across multiple scales using a desired filter kernel. If afforded by horizontal resolution, the filter scale can be selected to spatially vary with the local first baroclinic radius of deformation (Chelton et al. 1998). Applying this variable filter to geostrophic velocity results in estimates of EKE at scales less than those at which mesoscale eddies are expected to equilibrate, and also quantifies energy at scales greater than the deformation radius and within the realm of geostrophic turbulence. Selection



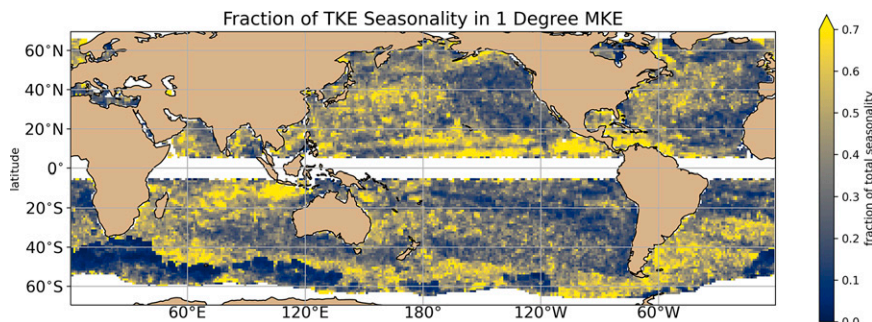


FIG. 9. Fraction of total KE seasonality resolved in  $1^\circ$  MKE estimate. This quantity is the ratio (filtered/total) of maximum–minimum KE across a seasonal cycle.

of a filter scale tied to a model grid scale, however, allows for direct comparisons between observations and models that have geographically varying grid scales. This may be particularly relevant for models that may only resolve eddies regionally, depending on their effective resolution relative to the local scale at which eddies equilibrate (Hallberg 2013).

As an example of how this filtering framework can be used to gauge resolved seasonality in a global climate model with relatively coarse resolution, we filter along-track velocities using a spatial filter kernel of width equal locally to  $1^\circ$  of longitude. Comparison of seasonality in the resulting MKE estimate to that of the unfiltered KE (Fig. 9) shows that while nearly  $\sim 60\%$  of the seasonal change in total KE is resolved in western boundary current regions, this is reduced to less than a third in the eastern half of the main ocean basins. Together with the observed seasonality in PE to EKE conversion that is greater than the annual mean, these results stress the need to implement time-varying parameterizations for energy conversion [such as Eq. (16)], as well as those for subgrid-scale EKE.

## 6. Conclusions

We identify stastically significant geographic and seasonal variations in EKE using a spatial filtering framework applied to along-track satellite altimeter derived estimates of geostrophic velocity. The partitioning of KE across spatial scales into mean and eddy components reveals a large fraction of total energy falls within the mesoscale band (60–300 km), varying with latitude and increasing with proximity to western boundary currents. This analysis also reveals that most regions of the ocean exhibit a winter-to-summer change in KE of  $\sim 20\%$  for scales of 60–140 km (Fig. 4), while seasonal peaks at 140–300-km scales occur over a range of months and depend on the local energy transfer pathways. These results highlight a scale-dependent seasonal cycle in EKE observed primarily at midlatitudes where large scales attain a seasonal maximum in the months following small scales, consistent with an inverse energy cascade.

The presence and seasonality of an inverse energy cascade is confirmed from concurrent estimates of seasonality in the conversion of PE to KE via mixed layer instability. The mean PE to EKE conversion rate, estimated via a parameterization (Fox-Kemper et al. 2008), is elevated at midlatitudes, with the peak conversion rate occurring typically in midwinter (Fig. 5).

At most locations the seasonal amplitude in this conversion rate is larger than its annual average.

Taken together, the temporal and geographic patterns of the PE to EKE conversion rate and EKE across spatial scales reveal a seasonally varying inverse cascade throughout the subtropical gyres. The geographic collocation of seasonality in each of these components of the energy cascade (conversion rate, small-scale, and large-scale EKE) as well as seasonal timing consistent with an energy cascade supports this conclusion. The timing in particular of PE to EKE conversion and maximum EKE at 60–140-km scales suggests KE released via mixed layer instability is a source of mesoscale KE moving upscale throughout late winter months. We have conservatively estimated the regions in which an inverse cascade occurs, and it is possible that some of the regions where a lag of zero months is observed also contain an energy cascade that occurs more rapidly than the regions identified here. We are able to identify regions where the total time lag between PE to EKE conversion and large-scale EKE is 1–6 months (0–2-month lag to small-scale EKE followed by a 1–4-month lag to large-scale EKE). While we are limited by the  $\sim 50$ -km resolution of along-track satellite observations, it may be possible that an inverse cascade exists at smaller spatial scales in some locations, particularly higher latitudes where the deformation radius is smaller. These results, specifically a scale-dependent seasonal cycle in EKE linked to seasonality in the conversion of PE to EKE, confirm similar seasonal energy cycles seen in high-resolution models (Uchida et al. 2017).

A widespread inverse cascade has implications spanning the water column. If some portion of wintertime submesoscale KE in the mixed layer energizes the mesoscale, then restratification of the mixed layer and related biological processes, like the springtime phytoplankton bloom, could depend on this inverse cascade and its time scale (Mahadevan et al. 2012). Where energy moves from smaller to larger horizontal scales, a similar cascade is also expected in the vertical, resulting in the barotropization, or transfer of energy to greater depths, of eddy vertical structures (Smith and Vallis 2001). Where barotropization is enhanced, so too may be bottom velocities that drive dissipation at the sea floor. In general, an improved understanding of processes controlling mesoscale energy levels, as well as cascade rates across space and time scales, is needed to predict and model ocean energetics. These questions, along with

investigations of the steady-state component of the inverse cascade, are left for future studies.

In addition to these results, the importance of a scale-aware view of the ocean's KE resides in its use as a validation metric for numerical models that resolve, partially resolve, or parameterize KE sources and sinks. The scale-aware and customizable nature of the one-dimensional analysis tool developed here provides the flexibility needed for a comprehensive evaluation of mesoscale processes in a range of numerical models. Using this tool to explore seasonality reveals the prevalence of an inverse cascade and stresses the importance of adequately resolving or parameterizing mesoscale eddy activity in global climate models. It is critical that energy in these models is properly partitioned across scales, locations, and seasons, as mesoscale turbulence redistributes heat and nutrients under the influence of changing large-scale circulation patterns.

**Acknowledgments.** This work was generously funded by NSF Grants OCE-1912302, OCE-1912125 (Drushka), and OCE-1912325 (Abernathey) as part of the Ocean Energy and Eddy Transport Climate Process Team. We thank Laure Zanna and the rest of the team for their feedback, guidance, and support.

**Data availability statement.** All altimeter measurements employed in this analysis can be obtained on Pangeo Pangeo Abernathey et al. (2021) (<https://catalog.pangeo.io/browse/master/ocean/altimetry/>) and are preprocessed for easy access. As presented here, filtering can be applied and scale-aware MKE and EKE estimated from *Jason-2*, *SARAL-AIka*, and *Sentinel-3A* along-track measurements using examples provided on GitHub ([https://github.com/ocean-eddy-cpt/WP1T2-2D-EKE-Analysis/along\\_track\\_filtering.ipynb](https://github.com/ocean-eddy-cpt/WP1T2-2D-EKE-Analysis/along_track_filtering.ipynb)). This repository also contains ready-made maps of EKE defined for various filter scales and types. Data files corresponding to filtering with Gaussian and taper filters in kilometers have been made available in NetCDF format (DOI: 10.5281/zenodo.6471003). Gridded climatology of upper-ocean density and mixed layer depth is generated from databases of Argo derived temperature and salinity profiles (Roemmich and Gilson 2009) ([http://sio-argo.ucsd.edu/RG\\_Climatology.html](http://sio-argo.ucsd.edu/RG_Climatology.html)), as well as mixed layer depths (Holte et al. 2017). These data were collected and made freely available by the International Argo Program and the national programs that contribute to it (<http://www.argo.ucsd.edu>). The Argo Program is part of the Global Ocean Observing System.

## REFERENCES

- Abernathey, R., and Coauthors, 2021: Cloud-native repositories for big scientific data. *Comput. Sci. Eng.*, **23**, 26–35, <https://doi.org/10.1109/MCSE.2021.3059437>.
- Aluie, H., M. Hecht, and G. Vallis, 2018: Mapping the energy cascade in the North Atlantic Ocean: The coarse-graining approach. *J. Phys. Oceanogr.*, **48**, 225–244, <https://doi.org/10.1175/JPO-D-17-0100.1>.
- Arbic, B., R. Scott, D. Chelton, J. Richman, and J. Shriver, 2012: Effects of stencil width on surface ocean geostrophic velocity and vorticity estimation from gridded satellite altimeter data. *J. Geophys. Res.*, **117**, C03029, <https://doi.org/10.1029/2011JC007367>.
- , K. Polzin, R. Scott, J. Richman, and J. Shriver, 2013: On eddy viscosity, energy cascades, and the horizontal resolution of gridded satellite altimeter products. *J. Phys. Oceanogr.*, **43**, 283–300, <https://doi.org/10.1175/JPO-D-11-0240.1>.
- , M. Muller, J. Richman, J. Shriver, A. Morten, R. Scott, G. Serazin, and T. Penduff, 2014: Geostrophic turbulence in the wavenumber-frequency domain: Eddy-driven low-frequency variability. *J. Phys. Oceanogr.*, **44**, 2050–2069, <https://doi.org/10.1175/JPO-D-13-054.1>.
- Callies, J., and R. Ferrari, 2013: Interpreting energy and tracer spectra of upper-ocean turbulence in the submesoscale range (1–200 km). *J. Phys. Oceanogr.*, **43**, 2456–2474, <https://doi.org/10.1175/JPO-D-13-063.1>.
- , —, J. Klymak, and J. Gula, 2015: Seasonality in submesoscale turbulence. *Nat. Commun.*, **6**, 6862, <https://doi.org/10.1038/ncomms7862>.
- , G. Flierl, R. Ferrari, and B. Fox-Kemper, 2016: The role of mixed-layer instabilities in submesoscale turbulence. *J. Fluid Mech.*, **788**, 5–41, <https://doi.org/10.1017/jfm.2015.700>.
- Charney, J., 1971: Geostrophic turbulence. *J. Atmos. Sci.*, **28**, 1087–1095, [https://doi.org/10.1175/1520-0469\(1971\)028<1087:GT>2.0.CO;2](https://doi.org/10.1175/1520-0469(1971)028<1087:GT>2.0.CO;2).
- Chelton, D., R. deSzoeke, M. Schlax, K. El Naggar, and N. Siwertz, 1998: Geographical variability of the first-baroclinic Rossby radius of deformation. *J. Phys. Oceanogr.*, **28**, 433–460, [https://doi.org/10.1175/1520-0485\(1998\)028<0433:GVOTFB>2.0.CO;2](https://doi.org/10.1175/1520-0485(1998)028<0433:GVOTFB>2.0.CO;2).
- , M. Schlax, R. Samelson, and R. de Szoeke, 2007: Global observations of large oceanic eddies. *Geophys. Res. Lett.*, **34**, L15606, <https://doi.org/10.1029/2007GL030812>.
- , —, —, and —, 2011: Global observations of nonlinear mesoscale eddies. *Prog. Oceanogr.*, **91**, 167–216, <https://doi.org/10.1016/j.pocean.2011.01.002>.
- Chen, S., and B. Qiu, 2021: Sea surface height variability in the 30–120 km wavelength band from altimetry along-track observations. *J. Geophys. Res. Oceans*, **126**, e2021JC017284, <https://doi.org/10.1029/2021JC017284>.
- Cole, S., K. Drushka, and R. Abernathey, 2020: Toward an observational synthesis of eddy energy in the global ocean. *CLIVAR Exchanges*, No. 77, International CLIVAR Project Office, Southampton, United Kingdom, 37–41, <https://doi.org/10.5065/g8w0-fy32>.
- Dong, J., B. Fox-Kemper, H. Zhang, and C. Dong, 2020a: The scale of submesoscale baroclinic instability globally. *J. Phys. Oceanogr.*, **50**, 2649–2667, <https://doi.org/10.1175/JPO-D-20-0043.1>.
- , —, —, and —, 2020b: The seasonality of submesoscale energy production, content, and cascade. *Geophys. Res. Lett.*, **47**, e2020GL087388, <https://doi.org/10.1029/2020GL087388>.
- Dufau, C., M. Orszynowicz, G. Dibarboure, R. Morrow, and P. Le Traon, 2016: Mesoscale resolution capability of altimetry: Present and future. *J. Geophys. Res. Oceans*, **121**, 4910–4927, <https://doi.org/10.1002/2015JC010904>.
- Ferrari, R., and C. Wunsch, 2009: Ocean circulation kinetic energy: Reservoirs, sources, sinks. *Annu. Rev. Fluid Mech.*, **41**, 253–282, <https://doi.org/10.1146/annurev.fluid.40.111406.102139>.
- Fox-Kemper, B., R. Ferrari, and R. Hallberg, 2008: Parameterization of mixed layer eddies. Part I: Theory and diagnosis. *J. Phys. Oceanogr.*, **38**, 1145–1165, <https://doi.org/10.1175/2007JPO3792.1>.
- , and Coauthors, 2011: Parameterization of mixed layer eddies. III: Implementation and impact in global ocean climate

- simulations. *Ocean Modell.*, **39**, 61–78, <https://doi.org/10.1016/j.ocemod.2010.09.002>.
- Germano, M., 1992: Turbulence: The filtering approach. *J. Fluid Mech.*, **238**, 325–336, <https://doi.org/10.1017/S0022112092001733>.
- Grooms, I., N. Loose, R. Abernathy, J. Steinberg, S. Bachman, G. Marques, A. Guillaumin, and E. Yankovsky, 2021: Diffusion-based smoothers for spatial filtering of gridded geophysical data. *J. Adv. Model. Earth Syst.*, **13**, e2021MS002552, <https://doi.org/10.1029/2021MS002552>.
- Hallberg, R., 2013: Using a resolution function to regulate parameterizations of oceanic mesoscale eddy effects. *Ocean Modell.*, **72**, 92–103, <https://doi.org/10.1016/j.ocemod.2013.08.007>.
- Holte, J., L. Talley, J. Gilson, and D. Roemmich, 2017: An Argo mixed layer climatology and database. *Geophys. Res. Lett.*, **44**, 5618–5626, <https://doi.org/10.1002/2017GL073426>.
- Johnson, L., C. Lee, and E. D’Asaro, 2016: Global estimates of lateral springtime restratification. *J. Phys. Oceanogr.*, **46**, 1555–1573, <https://doi.org/10.1175/JPO-D-15-0163.1>.
- Kraichnan, R., 1967: Inertial ranges in two-dimensional turbulence. *Phys. Fluids*, **10**, 1417–1423, <https://doi.org/10.1063/1.1762301>.
- Mahadevan, A., E. D’Asaro, C. Lee, and M. Perry, 2012: Eddy-driven stratification initiates North Atlantic spring phytoplankton blooms. *Science*, **337**, 54–58, <https://doi.org/10.1126/science.1218740>.
- Matano, R., C. Simionato, W. P. de Ruijter, P. J. van Leeuwen, P. T. Strub, D. B. Chelton, and M. G. Schlax, 1998: Seasonal variability in the Agulhas retroflection region. *Geophys. Res. Lett.*, **25**, 4361–4364, <https://doi.org/10.1029/1998GL900163>.
- McWilliams, J., 1989: Statistical properties of decaying geostrophic turbulence. *J. Fluid Mech.*, **198**, 199–230, <https://doi.org/10.1017/S0022112089000108>.
- Mensa, J., Z. Garraffo, A. Griffa, T. Ozgokmen, A. Haza, and M. Veneziani, 2013: Seasonality of the submesoscale dynamics in the Gulf Stream region. *Ocean Dyn.*, **63**, 923–941, <https://doi.org/10.1007/s10236-013-0633-1>.
- Pujol, M., and F. Mertz, 2020: Product User Manual for Sea Level SLA Products (CMEMS-SL-PUM-009-032-062). Copernicus Marine Environment Monitoring System, 52 pp.
- Qiu, B., S. Chen, P. Klein, and H. Sasaki, 2014: Seasonal mesoscale and submesoscale eddy variability along the North Pacific subtropical countercurrent. *J. Phys. Oceanogr.*, **44**, 3079–3098, <https://doi.org/10.1175/JPO-D-14-0071.1>.
- Risien, C. M., and D. B. Chelton, 2008: A global climatology of surface winds and surface wind stress fields from eight years of quikscat scatterometer data. *J. Phys. Oceanogr.*, **38**, 2379–2413, <https://doi.org/10.1175/2008JPO3881.1>.
- Rocha, C., T. Chereskin, S. Gille, and D. Menemenlis, 2016: Mesoscale to submesoscale wavenumber spectra in Drake Passage. *J. Phys. Oceanogr.*, **46**, 601–620, <https://doi.org/10.1175/JPO-D-15-0087.1>.
- Roemmich, D., and J. Gilson, 2009: The 2004–2008 mean and annual cycle of temperature, salinity, and steric height in the global ocean from the Argo platform. *Prog. Oceanogr.*, **82**, 81–100, <https://doi.org/10.1016/j.pocean.2009.03.004>.
- Roulet, G., J. McWilliams, X. Capet, and M. Molemaker, 2012: Properties of steady geostrophic turbulence with isopycnal outcropping. *J. Phys. Oceanogr.*, **42**, 18–38, <https://doi.org/10.1175/JPO-D-11-09.1>.
- Sadek, M., and H. Aluie, 2018: Extracting the spectrum by spatial filtering. *Phys. Rev. Fluids*, **3**, 124610, <https://doi.org/10.1103/PhysRevFluids.3.124610>.
- Sasaki, H., P. Klein, B. Qiu, and Y. Sasai, 2014: Impact of oceanic-scale interactions on the seasonal modulation of ocean dynamics by the atmosphere. *Nat. Commun.*, **5**, 5636, <https://doi.org/10.1038/ncomms6636>.
- Scharffenberg, M., and D. Stammer, 2010: Seasonal variations of the large-scale geostrophic flow field and eddy kinetic energy inferred from the TOPEX/Poseidon and JASON-1 tandem mission data. *J. Geophys. Res.*, **115**, 3523–3537, <https://doi.org/10.1029/2008JC005242>.
- Schubert, R., J. Gula, R. J. Greatbatch, B. Baschek, and A. Biastoch, 2020: The submesoscale kinetic energy cascade: Mesoscale absorption of submesoscale mixed layer eddies and frontal downscale fluxes. *J. Phys. Oceanogr.*, **50**, 2573–2589, <https://doi.org/10.1175/JPO-D-19-0311.1>.
- Scott, R., and F. Wang, 2005: Direct evidence of an oceanic inverse kinetic energy cascade from satellite altimetry. *J. Phys. Oceanogr.*, **35**, 1650–1666, <https://doi.org/10.1175/JPO2771.1>.
- , and B. Arbic, 2007: Spectral energy fluxes in geostrophic turbulence: Implications for ocean energetics. *J. Phys. Oceanogr.*, **37**, 673–688, <https://doi.org/10.1175/JPO3027.1>.
- Serazin, G., T. Penduff, B. Barnier, J. Molines, B. Arbic, M. Muller, and L. Terray, 2018: Inverse cascades of kinetic energy as a source of intrinsic variability: A global OGCM study. *J. Phys. Oceanogr.*, **48**, 1385–1408, <https://doi.org/10.1175/JPO-D-17-0136.1>.
- Smith, K., 2007: The geography of linear baroclinic instability on Earth’s oceans. *J. Mar. Res.*, **65**, 655–683, <https://doi.org/10.1357/002224007783649484>.
- , and G. Vallis, 2001: The scales and equilibrium of midocean eddies: Freely evolving flow. *J. Phys. Oceanogr.*, **31**, 554–571, [https://doi.org/10.1175/1520-0485\(2001\)031<0554:TSAEOM>2.0.CO;2](https://doi.org/10.1175/1520-0485(2001)031<0554:TSAEOM>2.0.CO;2).
- Stammer, D., and C. Dieterich, 1999: Space-borne measurements of the time-dependent geostrophic ocean flow field. *J. Atmos. Oceanic Technol.*, **16**, 1198–1207, [https://doi.org/10.1175/1520-0426\(1999\)016<1198:SBMOTT>2.0.CO;2](https://doi.org/10.1175/1520-0426(1999)016<1198:SBMOTT>2.0.CO;2).
- Taburet, G., M. Pujol, and SL-TAC Team, 2020: Quality information document: Sea level TAC-DUACS products (CMEMS-SL-QUID-008-032-062). Copernicus Marine Environment Monitoring System, 72 pp., <https://catalogue.marine.copernicus.eu/documents/QUID/CMEMS-SL-QUID-008-032-068.pdf>.
- Uchida, T., R. Abernathy, and S. Smith, 2017: Seasonality of eddy kinetic energy in an eddy permitting global climate model. *Ocean Modell.*, **118**, 41–58, <https://doi.org/10.1016/j.ocemod.2017.08.006>.
- Xu, Y., and L. Fu, 2012: The effects of altimeter instrument noise of the estimation of the wavenumber spectrum of sea surface height. *J. Phys. Oceanogr.*, **42**, 2229–2233, <https://doi.org/10.1175/JPO-D-12-0106.1>.
- Zanna, L., 2019: Proposal to CVP climate process teams on “ocean transport and eddy energy.” Figshare, 22 pp., <https://doi.org/10.6084/m9.figshare.10105922.v1>.
- Zhai, X., R. Greatbatch, and J. Kohlmann, 2008: On the seasonal variability of eddy kinetic energy in the Gulf Stream region. *Geophys. Res. Lett.*, **35**, L24609, <https://doi.org/10.1029/2008GL036412>.